Optics Letters

Silicon photonic microelectromechanical phase shifters for scalable programmable photonics

Pierre Edinger,[1] **Alain Yuji Takabayashi,**[2] **Carlos Errando-Herranz,**[1]
Umar Khan,[3] **Hamed Sattari,**[2] **Peter Verheyen,**[4] **Wim Bogaerts,**[3] **Niels Quack,**[2]
and Kristinn B. Gylfason[1,*]

[1]KTH Royal Institute of Technology, Stockholm, Sweden
[2]Ecole Polytechnique Fédérale de Lausanne, Switzerland
[3]Ghent University - IMEC, Department of Information Technology, Belgium
[4]Interuniversity Microelectronics Centre, Leuven, Belgium
*Corresponding author: gylfason@kth.se

Programmable photonic integrated circuits are emerging as an attractive platform for applications such as quantum information processing and artificial neural networks. However, current programmable circuits are limited in scalability by the lack of low-power and low-loss phase shifters in commercial foundries. Here, we demonstrate a compact phase shifter with low-power photonic microelectromechanical system (MEMS) actuation on a silicon photonics foundry platform (IMEC's iSiPP50G). The device attains $(2.9\pi \pm \pi)$ phase shift at 1550 nm, with an insertion loss of $(0.33^{+0.15}_{-0.10})$ dB, a V_π of $(10.7^{+2.2}_{-1.4})$ V, and an L_π of $(17.2^{+8.8}_{-4.3})$ μm. We also measured an actuation bandwidth $f_{-3\,dB}$ of 1.03 MHz in air. We believe that our demonstration of a low-loss and low-power photonic MEMS phase shifter implemented in silicon photonics foundry compatible technology lifts a main roadblock toward the scale-up of programmable photonic integrated circuits. © 2021 Optical Society of America under the terms of the OSA Open Access Publishing Agreement

Silicon photonics has in the last decade evolved from an academic curiosity to an essential piece of the global IT puzzle. Open-access silicon photonic foundries have democratized the deployment of photonic circuits, but the modest integration level achieved to date is far from its full potential. Current circuits using only tens to hundreds of active components while scaling to thousands and beyond are needed for versatile programmable photonics that could be used in telecommunications, quantum information processing, or artificial neural networks [1]. A major bottleneck for scaling is the power consumption of these active components. Current phase shifters and couplers rely on thermo-optic tuning and consume milliwatts to tens of milliwatts each [2]. Thermal cross talk between such components puts a hard limit on the achievable integration density. In contrast, micro-electro-mechanical systems (MEMS) use less than a μW of power for their electrostatic

actuators and enable continued scaling of silicon photonic circuits [3]. Photonic MEMS devices have shown low insertion loss (IL), footprints on par with thermo-optic counterparts, and faster response times up to several MHz [4] without thermal cross talk. Moreover, silicon MEMS technology has already matured into well-established platforms and benefits from similar process development as electronics and silicon photonics [5]. MEMS do not exist as standard silicon photonics foundry components yet, although their scaling potential has already been demonstrated, for example, by a 240×240 digital switch matrix [6]. However, for multipurpose, programmable photonics, analog control over coupling (0–100%) and phase shift ($\geq 2\pi$) are needed as well. Silicon photonic MEMS phase shifters have been demonstrated on bare silicon-on-insulator (SOI) wafers [7–9], exhibiting >0.5 dB IL, and a limited speed due to a lack of doping or low-resistance metal routing. MEMS phase shifters employing gold for their actuators have achieved faster
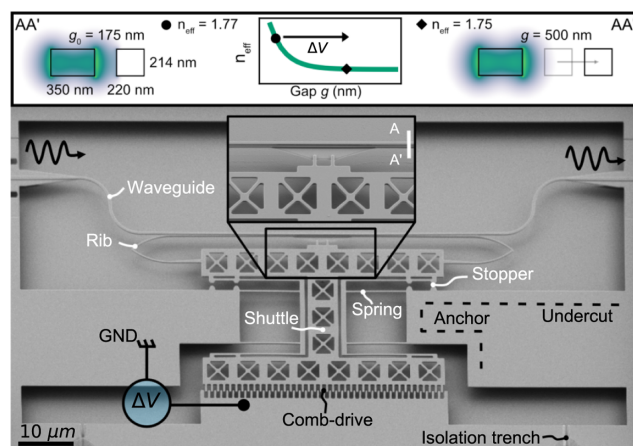
Fig. 1. SEM top-view of our low-power MEMS phase shifter for scalable programmable circuits. Inset, simulated E-field magnitude of the TE mode guided in the phase shifting cross section at two actuation points and a graph of the simulated effective mode index with respect to gap width.

speeds, such as a hybrid Si/Au ring resonator and SiN/Au phase shifters, but at the cost of foundry compatibility [4,10,11]. Similar devices for optomechanics have been implemented on AIM's passive SiN foundry platform but still required custom deposition of metal for MEMS actuation [12]. Recently, a slot waveguide phase shifter was shown on post-processed dies from GlobalFoundries's CMS90WG platform, reporting very low passive IL but with an expected increase in IL with actuation [13].

In this work, we experimentally demonstrate a silicon photonic MEMS phase shifter implemented in a standard foundry platform that achieves more than 2π phase shift at 1550 nm, with low IL. The device displays good phase shift linearity and operates in air up to a $f_{-3\,\mathrm{dB}}$ cutoff frequency of 1.03 MHz. The length of the phase-shifting section is only 50 μm, with an overall device footprint of 100×45 μm^2.

Figure 1 presents our photonic MEMS phase shifter. The device relies on geometrical modification of the modal cross section of a suspended silicon waveguide, achieved with a MEMS comb-drive actuator. A voltage bias V is applied between the movable H-shaped shuttle (GND) and the fixed anchored electrode. The bias induces an attractive force in the comb-drive actuator, reducing the distance between both sets of teeth and displacing the free-hanging shuttle. A 220 nm wide and 50 μm long silicon rib attached to the shuttle is, thus, pulled away from the fixed suspended waveguide. A phase shift $\Delta\phi$ at a given wavelength λ is obtained due to the change of effective index n_{eff} of the guided mode induced by the geometrical tuning, according to

$$\Delta\phi(V, \lambda) = \frac{2\pi L (n_{\mathrm{eff}}(g(V), \lambda) - n_{\mathrm{eff},0}(\lambda))}{\lambda}, \qquad \textbf{(1)}$$

with L being the length of the phase shifting section, $n_{\mathrm{eff},0}$ being the waveguide effective index in the OFF-state, and $n_{\mathrm{eff}}(g(V), \lambda)$ being a function composition, where the effective index varies exponentially with the waveguide gap g; see the graph inset in Fig. 1. The waveguide gap g, in turn, depends on the applied voltage V and is approximated as

$$g(V) \approx g_0 + \frac{1}{k}\epsilon\, N_{\mathrm{F}} \frac{t}{g_{\mathrm{CD}}} V^2, \qquad \textbf{(2)}$$

with g_0 being the initial waveguide gap, k being the actuator's spring constant in the direction of motion, ϵ being the dielectric constant of air, N_{F} being the number of electrode fingers of the

comb-drive actuator, t being the device layer thickness, and g_{CD} being the finger gap [14]. The change in gap is, therefore, proportional to the square of the voltage. With small gaps, large changes in effective index can be achieved with minimal displacement, and a gap-reducing configuration could reach large phase shifts by shrinking the initial gap below the lithography minimum feature size. However, the response curve is then strongly non-linear, due to the combined contributions of the exponential $n_{\mathrm{eff}}(g)$ and $g \propto V^2$.

In our device, we instead increase the gap to obtain a phase response curve with improved linearity. At low voltages, a large change in the effective index is achieved with small displacements. At higher voltages, the larger displacements compensate for the diminishing change in effective index at wider gaps; see Supplement 1. By using a comb-drive actuator, we reach in-plane displacements of 500 nm, and mechanical stoppers eliminate pull-in risk. We use bends in the suspended waveguide and folded springs to avoid buckling associated with relaxation of residual compressive strain upon release of the Si device layer of the SOI substrate. A central 50 μm long, 350 nm wide section of the suspended waveguide overlaps with the narrow n_{eff} tuning rib that is attached to the movable shuttle in three points. The restoring force is provided by four folded springs, composed of individual 10 μm long and 300 nm wide beams, resulting in an overall stiffness along the direction of motion of 2 N/m. We designed the initial waveguide gap as 175 nm, and—combined with the 500 nm of displacement and 50 μm of active waveguide length—the device targets 2π phase shift with 30 V actuation at 1550 nm. Finally, the calculated mass of the H-shaped shuttle is 0.177 ng, from which we estimate a mechanical resonance frequency of 535 kHz.

We implemented our MEMS phase shifters on IMEC's iSiPP50G silicon photonics platform, followed by a few post-processing steps to release the actuator and waveguide [15]. To prepare for MEMS cavities, we used a back-end-of-line (BEOL) opening module of the iSiPP50G platform to locally remove the oxide stack and expose the device layer. Then, we used a buffered hydrofluoric acid (HF) solution to remove the remaining lateral cladding oxide around the waveguides. To protect the other parts of the silicon photonics chip, such as the grating couplers and BEOL layer stack, we deposited a 50 nm conformal alumina layer and selectively opened it over the electrical bond pads and MEMS cavities. In the last step, we used vapor HF to etch away the buried oxide lower cladding, releasing the MEMS for
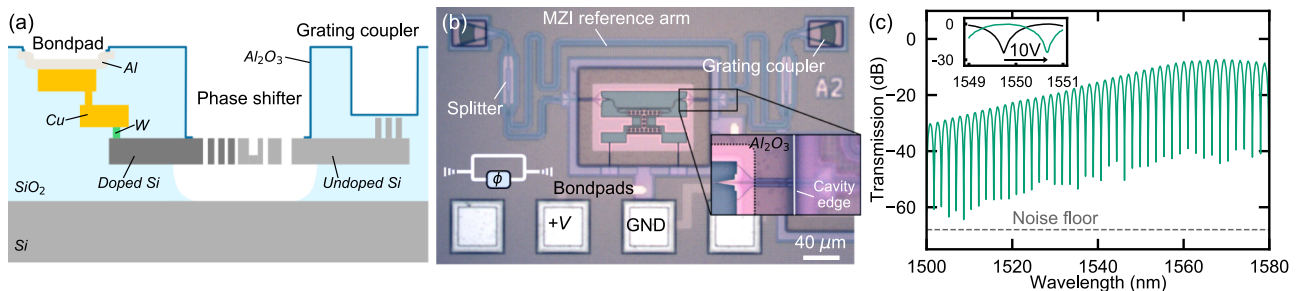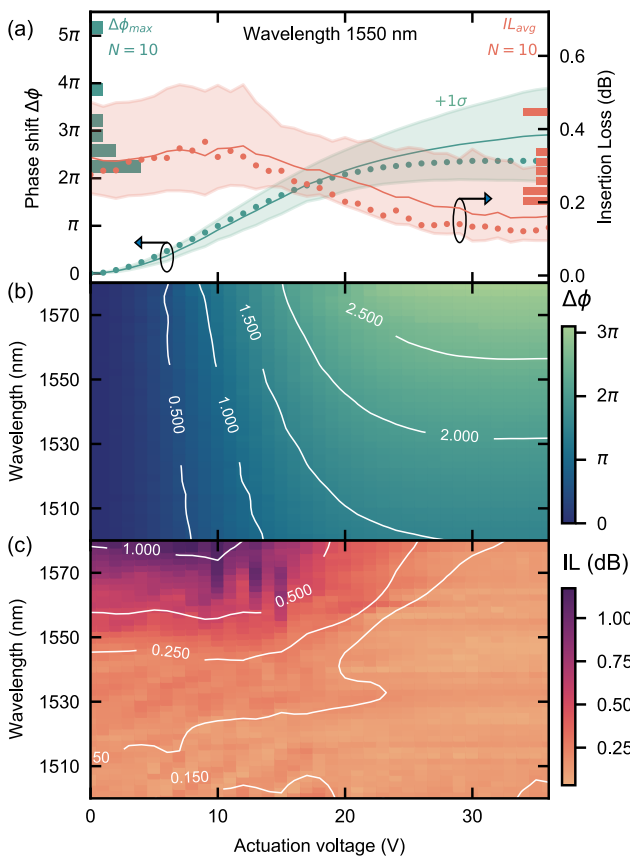

Fig. 2. Implementation of a photonic MEMS phase shifter on the iSiPP50G platform. (a) Sketch of the final cross section, combining electrical and photonic layers from the foundry with suspended Si structures. (b) A fabricated phase shifter within an MZI, interfaced using standard grating couplers and bond pads from the platform library. Inset, optical microscope close-up view of an oxide-air waveguide transition. (c) Measured transmission spectrum, which was fitted to extract both phase shift and insertion loss versus voltage. Inset, enlarged view around 1550 nm and an example of the spectrum shift with actuation.

actuation. The release leaves a 3 μm undercut of the Si. The final cross section is shown schematically in Fig. 2(a).

We used an on-chip Mach–Zehnder interferometer (MZI) circuit for optomechanical characterization; see Fig. 2(b). The circuit uses multimode interference (MMI) splitters, grating couplers, and bond pads from the iSiPP50G design kit. We evaluated the phase shifter in the wavelength range from 1500 to 1580 nm and fitted each fringe to extract both the phase shift $\Delta\phi$ and the device IL; see Supplement 1. In Fig. 2(c), we show an example transmission spectrum, with an inset enlarged view of a single fringe shift with actuation.

We characterized the phase shifter under static conditions over the entire wavelength range by applying DC bias from 0 to 36 V. In Fig. 3(a), we show the extracted $\Delta\phi$ and IL at 1550 nm for 10 device copies (for details on the samples and statistics; see Supplement 1). All phase shifters reach the intended 2π threshold with good linearity, with a maximum $\Delta\phi$ of $(2.9\pi \pm \pi)$ at 36 V, and a V_π of $(10.7^{+2.2}_{-1.4})$ V. The device IL is $(0.33^{+0.15}_{-0.10})$ dB in the OFF-state and decreases to $(0.16^{+0.14}_{-0.07})$ dB at maximum $\Delta\phi$. Figures 3(b) and 3(c) show the dispersion of $\Delta\phi$ and IL, respectively, for a representative device indicated by dotted lines in Fig. 3(a). The device attains at least 1.5π phase shift over the full wavelength range and 2π from 1532 nm upward. The losses plotted are those of the devices themselves, not

including the oxide-to-air transition losses, which we independently measured as (0.036 ± 0.004) dB per transition at 1550 nm; see Supplement 1. For all devices, we remeasured the 0 V transmission in between all voltage steps and did not observe any hysteresis. Additionally, we measured a phase shifter without intermediate 0 V steps and verified that the response is the same when increasing and decreasing the voltage; see Supplement 1. The device could be actuated beyond contact with the mechanical stoppers without sign of damage or hysteresis.

We also measured the frequency response of the actuator in ambient air; see Fig. 4. We applied a modulated sine voltage $V_{DC} \pm v_{AC} \cos(\omega t)$ to the fixed electrode of the comb-drive and used a lock-in amplifier to read out the modulated output signal from the MZI test circuit. We fixed the wavelength to 1550.3 nm, which we measured to be at -3 dB from a fringe maximum at 0 V. In Fig. 4(a), we show both normalized modulation and mechanical phase offset from the drive at 5 V DC bias and a modulation amplitude v_{AC} of 0.5 V, from 10 kHz to 2 MHz. The output modulation was normalized to the value at 10 kHz. The device was measured in air, which induces some damping, but a resonance could clearly be observed at 503 kHz, and the $f_{-3\,dB}$ value was extracted as 1.03 MHz. We confirmed the response for different V_{DC} from 1 to 9 V, keeping v_{AC} fixed at 0.5 V; see Fig. 4(b). Finally, we measured a rise time of 2.0 μs and a fall time of 9.6 μs with a square modulation. We also measured a power consumption lower than 1 nW for π-modulation at 1 kHz; see Supplement 1. All measurement data can be found in Dataset 1, Ref. [16].

Our device attains a phase shift over 2π, as intended, and at a lower voltage of 20 V than the predicted 30 V. The difference can be due to a deviation from designed to fabricated geometry (e.g., a softer, narrower spring, as $k \propto w_s^3$, with w_s the spring width), and/or to oversimplification in the design model (e.g., neglect of fringing fields and assumption of fully clamped springs). The device IL typically decreases with actuation, which we attribute to a decrease in scattering as the field
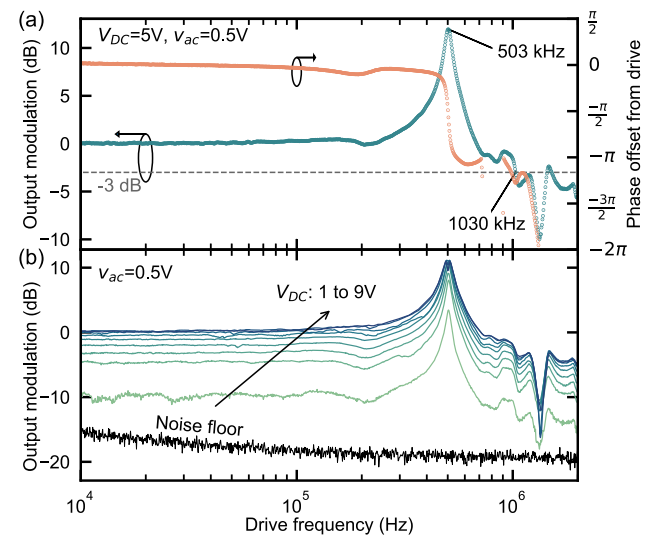
Fig. 3. DC characterization of our photonic MEMS phase shifter. (a) Extracted phase shift $\Delta\phi$ and insertion loss (IL) with respect to voltage at a wavelength of 1550 nm. Ten devices were measured on different dies from different wafers. The bars on the left and right are histograms of maximum $\Delta\phi$ and average IL, respectively. Measured (b) phase shift and (c) insertion loss (IL) from 1500 to 1580 nm, up to 36 V actuation, for the device indicated by the dotted lines in (a).

Fig. 4. AC opto-mechanical characterization in ambient air of the photonic MEMS phase shifter highlighted in Fig. 3. (a) Normalized output modulation of the MZI (left axis), and phase offset from the drive (right axis) with a DC bias of 5 V and drive modulation of 1 V_{pp}. (b) Normalized output modulation for different DC biases at a fixed modulation of 1 V_{pp}.

Table 1. Performance Comparison of Silicon Photonic MEMS Shifters

Platform	$\Delta\phi_{max}$ (π)	IL_{min} (dB)	IL_{max} (dB)	L_{π} (μm)	V_{π} (V)	$f_{-3\,dB}$ (MHz)	Reference
iSiPP50G[a]	2.9	0.16	0.33	17.2	10.7	1.03	Here
SOI	2.27	0.58	0.58[b]	7.7	11	–	[8]
SOI	0.9[b]	1.3[b]	–	279[b]	–	–	[9]
CMS90WG[a]	1.79	0.04	–	14	0.85	0.26	[13]
Si/Au	0.25[b]	0.33[b]	–	51[b]	–	2	[4]
SiN/Au	1.5	0.01[b]	0.1	67[b]	33	–	[10]
SiN/Au	2	0.47	0.47[b]	75	5.6	2.85	[11]

[a]Post-processing steps outside of the foundry needed to release the MEMS.
[b]Calculated values; see Supplement 1.

overlap with the waveguide sidewall being reduced. The field intensity is high along the sidewall at small gaps, and scattering due to roughness is significant, despite the short phase-shifting section. The effect is stronger at longer wavelengths due to the lower mode confinement. A spread in maximum $\Delta\phi$ and IL can be observed, which we mainly attribute to wafer-to-wafer variations in waveguide dimensions. A deviation of ±10 nm can be expected in waveguide widths and of ±20 nm for the air gaps. As efficient evanescent tuning relies on low mode confinement, such small variations in waveguide dimensions can lead to a significant spread in $\Delta\phi$ and IL. Compared to other reported silicon photonics MEMS phase shifters, in terms of the performance metrics in Table 1, our device offers a good balance between IL, maximum phase shift, speed, and footprint. When compared only to devices using the Si device layer of SOI wafers, our device exhibits the largest $\Delta\phi_{max}$ and $f_{-3\,dB}$ reported, with good IL, L_{π}, and V_{π} as well. Only the recently published dual-slot phase shifter reports a lower IL on a 160 nm SOI CMOS platform, although we expect the value to increase with actuation. In an extended comparison with recently reported photonic MEMS phase shifters on other material platforms, we find three designs with overall good performance but different trade-offs, particularly favoring a specific figure of merit. However, all those devices rely on additional conductive layers in the actuators. Our phase shifter, in contrast, was produced in a commercial foundry process providing two-level metal interconnects and high-speed optoelectronic modulators and detectors. A few post-processing steps are still needed to release our MEMS device, but all steps are compatible with wafer-scale fabrication and could be implemented in the foundry. In combination with high-voltage CMOS driving electronics and wafer-scale packaging solutions [17], our phase shifter can be used to build large-scale MEMS-based programmable photonic circuits. The performance is also expected to improve in circuits by combining multiple devices into single MEMS cavities and, thus, reducing the overall footprint and IL as fewer oxide-air transitions are needed. However, further analysis of variations in performance and general yield is required for commercialization. Beyond the present work, we expect the scalability metrics of MEMS phase shifters to benefit from future improvements in lithography capability of photonic foundries. Both the electrostatic force and the effective index tuning scale beneficially with reduced feature size, which will lower V_{π} and reduce the actuator footprints.

We believe that our phase shifter presents a crucial step toward large-scale programmable photonic circuits because of its low power consumption, low loss, and small footprint. Moreover, with a -3 dB bandwidth of 1.03 MHz, the phase shifter is an order of magnitude faster than available thermo-optic counterparts. Finally, our implementation on a photonic foundry platform that includes optoelectronics and metal routing enables dense MEMS-enhanced photonic circuits, paving the way toward complex and large-scale programmable photonics.

Disclosures. The authors declare no conflicts of interest.

Data Availability. Measurement data available in Dataset 1, Ref. [16].

Supplemental document. See Supplement 1 for supporting content.

REFERENCES

1. W. Bogaerts, D. Pérez, J. Capmany, D. A. B. Miller, J. Poon, D. Englund, F. Morichetti, and A. Melloni, Nature **586**, 207 (2020).
2. S. Chung, M. Nakai, and H. Hashemi, Opt. Express **27**, 13430 (2019).
3. C. Errando-Herranz, A. Y. Takabayashi, P. Edinger, H. Sattari, K. B. Gylfason, and N. Quack, IEEE J. Sel. Top. Quantum Electron. **26**, 1 (2020).
4. C. Haffner, A. Joerg, M. Doderer, F. Mayor, D. Chelladurai, Y. Fedoryshyn, C. I. Roman, M. Mazur, M. Burla, H. J. Lezec, V. A. Aksyuk, and J. Leuthold, Science **366**, 860 (2019).
5. H. Qu, Micromachines **7**, 14 (2016).
6. T. J. Seok, K. Kwon, J. Henriksson, J. Luo, and M. C. Wu, Optica **6**, 490 (2019).
7. K. V. Acoleyen, J. Roels, P. Mechet, T. Claes, D. V. Thourhout, and R. Baets, IEEE Photon. J. **4**, 779 (2012).
8. H. M. Chu and K. Hane, IEEE Photon. Technol. Lett. **26**, 1411 (2014).
9. C. Errando-Herranz, F. Niklaus, G. Stemme, and K. B. Gylfason, Opt. Lett. **40**, 3556 (2015).
10. M. W. Pruessner, D. Park, T. H. Stievater, D. A. Kozak, and W. S. Rabinovich, Opt. Express **24**, 13917 (2016).
11. T. Grottke, W. Hartmann, C. Schuck, and W. H. P. Pernice, Opt. Express **29**, 5525 (2021).
12. M. W. Pruessner, D. A. Kozak, N. A. Tyndall, W. S. Rabinovich, and T. H. Stievater, OSA Contin. **4**, 1215 (2021).
13. R. Baghdadi, M. Gould, S. Gupta, M. Tymchenko, D. Bunandar, C. Ramey, and N. C. Harris, Opt. Express **29**, 19113 (2021).
14. R. Legtenberg, A. W. Groeneveld, and M. Elwenspoek, J. Micromech. Microeng. **6**, 320 (1996).
15. A. Y. Takabayashi, H. Sattari, P. Edinger, P. Verheyen, K. B. Gylfason, W. Bogaerts, and N. Quack, J. Microelectromech. Syst. **30**, 322 (2021).
16. P. Edinger, U. Khan, and K. B. Gylfason, "Raw data for silicon photonic MEMS phase shifters for scalable programmable photonic circuits," figshare, 2021, https://doi.org/10.6084/m9.figshare.16823023.
17. G. Jo, P. Edinger, S. J. Bleiker, X. Wang, A. Y. Takabayashi, H. Sattari, N. Quack, M. Jezzini, P. Verheyen, G. Stemme, W. Bogaerts, K. B. Gylfason, and F. Niklaus, Proc. SPIE **11691**, 116910E (2021).